Viscous roots of active seismogenic faults revealed by geologic slip rate variations

P. A. Cowie[1], C. H. Scholz[2], G. P. Roberts[3], J. P. Faure Walker[4] and P. Steer[1,5]

1. Department of Earth Science, University of Bergen, Bergen 5002, Norway

2. Lamont Doherty Earth Observatory of Columbia University, Palisades, NY 10964-8000, USA

3. School of Earth Sciences, Birkbeck College, University of London, WC1E 7HX, UK

4. Institute for Risk and Disaster Reduction, University College London, London, WC1E 6BT, UK

5. Géosciences Rennes, Université de Rennes 1, CNRS, Rennes Cedex CS 35042, France.

During the earthquake cycle viscous flow at depth contributes to elastic strain accumulation along seismogenic faults[1]. Evaluating the importance of this contribution to fault loading is hampered by uncertainty about whether viscous deformation mainly occurs in shear zones or by distributed flow. Furthermore, viscous strain rate has a power-law dependence on applied stress[2] but few estimates exist for the power-law exponent applicable to the long term in situ behaviour of active faults. Here we show that measurements of topography and whole-Holocene offsets along seismically active normal faults in the Italian Apennines can be used to derive a relationship between stress and strain rate (averaged over 15±3 kyrs). This relationship, which follows a well-defined power-law with an exponent in the range 3.0-3.3 (1σ), is used to infer the rheological structure of the crust and constrain the width of active extension across the Apennines. Our result supports the idea that the irregular, stick-slip movement of upper crustal faults, and hence earthquake recurrence, are controlled by down-dip viscous flow in shear zones over multiple earthquake cycles.

Earthquakes in the crust occur down to depths of approximately 15km in most regions because below this depth temperature- and time-dependent creep (aseismic) deformation processes become progressively more important. It is therefore generally accepted that the upper crustal, seismogenic, portion of a fault is rooted down dip into a ductile (mylonitic) shear zone and that the transition from frictional stick-slip to viscous flow is temperature and strain rate dependent. At sufficiently high temperatures, distributed ductile deformation may also occur in the lower crust and upper mantle. *Both* localised flow in shear zones and distributed flow lead to elastic strain accumulation in the upper crust and thus loading of faults to failure but currently there is disagreement as to which dominates[3,4]. Experimental work, field data and theory indicate the flow law for the lithosphere at tectonic strain rates should be that of dislocation creep in which strain rate, $\dot{e}$, is proportional to stress raised to an exponent n, where n is typically in the range 2 to 4[5,6]:

$$\dot{e} = A\sigma^n \exp\left(-Q/RT\right) \qquad \text{Equation 1}$$

Here σ is driving stress, A is a material property, Q is activation energy, R is the molar gas constant and T is absolute temperature. Geodetic observations of post-seismic relaxation reveal temporal and spatial variations in effective viscosity that are most easily explained by power law creep with $n \approx 3$[7]. However geodetic data generally do not permit discrimination between contributions of bulk flow of the upper mantle, of the lower crust, or plastic creep within a shear zone[2]. Moreover, it is not clear that the rheological properties indicated by postseismic transients are applicable to longer term behaviour of the coupled frictional-viscous fault system[8].

Here we show that extensional strain rates derived from slip on seismogenic normal faults in the actively uplifting and extending central and southern Italian Apennines can be

used to address this issue. The strain rates are measured at the surface using published structural data[9,11] (Fig. 1, 2; see Methods) along active normal faults, characterised by bedrock scarps that exhibit striated fault planes and offset dated Holocene sediments and geomorphic surfaces[11]. These faults have developed in the last 2-3 My since thrusting in this region diminished as westward subduction of the Adriatic plate beneath the Italian peninsula slowed and slab tearing/detachment initiated ~6 Ma[10,12]. Present day topographic elevation increases inland reaching elevations up to 2900 m locally along the footwall crests of major extensional faults. Short wavelength (10-20 km) topographic variations due to faulting are superimposed on long wavelength (100-150 km) topography aligned NW-SE along the axis of the Italian Peninsula[12] (Fig. 2a). Gravity admittance data indicate that the long wavelength topography is supported by buoyancy variations in the uppermost mantle[12]. Regional surface uplift rates[13] increase in magnitude inwards from the Adriatic and Tyrrhenian coasts, mimicking in shape the long wavelength topography[13].

The extensional strain rates, averaged over the whole Holocene (15±3 kyrs), correlate with average topographic elevation along the length of the central and southern Apennines[10] (Fig. 1c). This observation is confirmed by the map view distribution of active faults relative to topographic contours (e.g., Fig. 2a). Geodetic data also show that the highest contemporary strain rates coincide with the highest elevation area in the central Apennines[14]. A power law regression between the strain rate, $\dot{e}$, and elevations, h, (in transects 90 km across strike by 30 km wide along strike) reveals a well-defined relationship with power law exponents in the range 3.0-3.3 (1σ) (see Methods and Supplementary material). Data from two independent sets of 30km transects show that the result is not location dependent (Fig. 1d). Varying transect width (from 5 km to 60 km) shows that over all scales the exponent lies within the range 2.7-3.4 and 2.3-4.0 at 95% and 99% confidence intervals respectively. These variations

in strain rate cannot be attributed to thermal structure as heat flow increases gradually from < 40 mWm^{-2} along the Adriatic coast to > 60 mWm^{-2} along the Tyrrhenian coast, independent of elevation and distance along strike[15].

To interpret our data (Fig. 1d) in terms of Equation 1 we need to demonstrate that h and σ are directly proportional. Previous workers (e.g., ref **16**) made the connection by approximating the lithosphere as a homogeneous thin viscous sheet. However, where thicker than average crust (40 – 50km) overlies thinned mantle lithosphere, as it does in the central and southern Apennines, the vertical velocity field is unlikely to be continuous at the scale of the entire lithosphere[17]. Furthermore, the topography varies by 100's of meters over wavelengths < 100 km in which case approximations made in the thin sheet model break down[18]. To avoid making these approximations we use observational constraints to relate h to σ by noting that (1) the upper crust is at or close to the threshold for brittle failure, i.e., "at yield"[19] and (2) earthquake focal mechanisms and fault kinematic data along active faults[9,11] indicate that the maximum compressive stress, σ_1, is vertical and the least compressive stress σ_3 is parallel to the principal extensional strain orientation (NE-SW in Fig. 2). In an elastic-brittle upper crust at yield, σ_3, is directly proportional to σ_1, compatible with incipient frictional failure on optimally oriented planes[20] (Fig. 3). Thus the differential stress is also proportional to σ_1, e.g., $(\sigma_1 - \sigma_3) \approx 2\sigma_1/3$ if Byerlee friction constants are assumed. Below the base of the seismogenic zone (~14-17 km depth in this region[19,21]), where viscous flow dominates, differential stress is less but we assume there is no stress discontinuity across this transition over long time scales (Fig. 3). Additional topographic loads that result from surface uplift relative to sea level increase σ_1, and hence $(\sigma_1 - \sigma_3)$, driving deformation (by a depth and temperature dependent combination of frictional slip and viscous flow; Fig. 3) such that differential stress in the upper crust is relaxed to re-establish the "at yield" condition (Fig.

94 3c). As both frictional and viscous components of the fault system undergo the same overall
95 strain, they operate in parallel (A, B in Fig. 3b). As long as surface uplift since extension
96 began is proportional to elevation, h, which as explained in the Methods is a reasonable
97 assumption[10,12], the increase in differential stress is independent of depth and simply
98 proportional to ρgh (ρ is crustal density; g is acceleration due to gravity). This reasoning,
99 which requires that buoyancy forces rather than plate boundary forces are the dominant
100 control on upper crustal deformation, explains the spatial variation in regional strain rates,
101 provides the link between the relationship shown in Fig. 1(d) and Equation 1, and thereby
102 allows us to constrain the exponent $n \approx 3$. Other studies that compare topography with strain
103 rates derived from fault slip and geodetic data[16] assume $n \approx 3$ to explain their data but here,
104 for the first time, we use such data to constrain its value.

105 Our surface strain rate measurements are derived from slip along faults so they do not
106 represent deformation of a continuum. For example, at the scale of individual fault blocks
107 (20km x 20km; Fig. 2a) the spatial gradients in strain rate and mean elevation (Fig. 2b) co-
108 vary, consistent with the regional relationship (Fig. 1), but the correlation between $\dot{e}$ and h is
109 poor ($R^2 < 0.5$) because of the heterogeneous pattern of brittle faulting. However, is viscous
110 deformation at depth also likely to be heterogeneous, as proposed in Fig. 3(a)? Deforming
111 non-linear viscous materials (i.e. $n > 1$), in general, show a tendency to localise strain and the
112 development of a brittle fault up-dip provides a geometrical discontinuity that influences
113 where in the viscous regime localisation preferentially develops[22]. Brittle-frictional faults
114 extending down to depths of at least 10km in this area are revealed by earthquake
115 aftershocks[21]. During major earthquakes, cataclasis, hydrous alteration and shear heating
116 together contribute to grain size reduction and material weakening[8], processes associated with
117 localisation at the frictional-viscous transition[23] (Fig. 3) and enhanced shear zone

development within the viscous regime down-dip of seismogenic faults[24]. We also know that fine grained, poly-mineralic, mylonitic shear zones remain weaker[23] and deform at higher strain rates than surrounding coarser grained less deformed rock (red line, Fig. 3a) and contribute to lowering the effective viscosity (Fig. 1d)[25].

In the mid- to lower crust quartzo-feldspathic mylonites form a fabric of mineral segregated layers parallel to shear so that their strength is controlled by the weakest phase: quartz. Using a flow law for wet quartz calibrated for mylonitic rocks[26] to fit measured strain rates across brittle fault zones (~5 km wide)[9], we estimate a lower bound on the temperature, T, of the viscously deforming material to be 710±120K (~440 ±120°C). These temperatures are reached just below the base of the seismogenic zone (25±7.5 km), as constrained by surface heat flow data[15] and upper crustal seismicity[19,21] (see Methods). At the 99% confidence level the exponent we derive is consistent with this flow law (Fig. 1d) as well as with recent theoretical predictions of shear zone rheology[27] and textural evidence[8,23,25,26,27] from poly-mineralic mylonitic rocks. We suggest therefore that the rate of viscous flow in shear zones dominates over distributed flow within the lower crust and/or upper mantle and regulates the slip rate we measure over long timescales on the up-dip seismogenic part of the fault even if on shorter time scales rupture depends on elastic loading and mechanical instabilities[3,4].

The relationship between $\dot{e}$ and h (Fig. 1d) also permits the controls on regional seismic hazard to be re-evaluated. Uplift of the Italian Peninsula has been on-going since at least the Quaternary, fast enough in places to raise Plio-Pleistocene marine sediments by over 400 m since the Early Pleistocene[10,28,29]. Contemporary surface uplift, documented by geodetic levelling lines across both the footwalls and hanging-walls of active faults, indicates regional uplift of 0–0.5 mm/yr close to the coasts, increasing to 1.0–1.5 mm/yr inland[13].

142 Furthermore, slip rates along the largest normal faults in the highest elevation areas of central
143 Italy (Fig. 2a) increased significantly ~0.8-1Ma[30]. Some hanging-wall basins became
144 internally drained[12] in part because of high rates on basin-bounding faults, consistent with
145 progressive strain localisation[14,30]. Although recent analysis of geodetic data and instrumental
146 seismicity suggests that active deformation may be localised in a zone only ~50km wide[14]
147 (Fig. 4), historical earthquake shaking records (since 1349 A.D.) and the distribution of
148 Holocene scarps imply a broader active zone 80-90km wide (Fig. 4). These apparently
149 contradictory observations become consistent when viewed in the light of the derived
150 relationship (Fig. 1d) as it predicts that strain rate decreases rapidly across strike from the
151 highest elevation areas towards the coast (Fig. 4) and smaller strains are more readily
152 resolved when observed over a longer period of observation (10^2-10^4 yr versus < 10^1 yr in
153 this case).

154 In summary, rates of seismicity on frictional faults in this example are regulated by
155 rates of localised viscous flow at depth constrained for the first time by observations averaged
156 over the timescale of multiple earthquake cycles and likely representing the *in situ* and long-
157 term (10^4 years) mechanical properties of deforming mylonitic shear zones.

158 **Methods:**

159 **Strain rate calculation:** Reference **9** presents the calculations used to convert field
160 measurements of the direction and amount of Holocene fault slip (since 15±3 ka) into strain-
161 rates within grid cells, the dimensions of which can be specified and thus varied. Fig. 2(a)
162 shows principal extensional strain rates (blue bars) calculated using this approach for 20 km x
163 20 km grid cells for the central Apennines. The strain rate calculations follow established
164 methods. For details see Supplementary material. To obtain the strain rate data shown in Fig.
165 1 the principal extensional strain rate is first calculated using a 5 km × 5 km grid oriented

NE-SW, approximately parallel to the principal strain orientation (043°-223°), extending a distance 90 km across strike. From these data we calculate the strain rate in adjacent rectangular regions 5km x 90km (see Fig. S1 in Supplementary material). We combine together adjacent 5km x 90km regions to obtain independent estimates of the principal strain rate in transects of a given width (10km, 20km, 30km etc.; Fig. S2) over the whole study area. Transects 30km wide suppress short length scale variations due to fault displacement gradients and constrain well the regional variations in strain rate along strike along the Italian Apennines from NW to SE (see Fig. S2). To characterise shorter wavelength spatial variations in strain rate and elevation across strike across the central Apennines we calculate $\Delta\dot{e} / \Delta x$ and $\Delta h / \Delta x$ (Fig. 2b), by taking the difference in strain-rate ($\Delta\dot{e}$) and mean elevation (Δh) between adjacent 20 km x 20 km cells (Fig. 2a) along the extension direction (043°-223°), from NE to SW, and dividing by Δx = 20 km.

Topographic data and stress: To calculate elevation (Fig. 1) topographic profiles located along the centre of 5 km x 90 km regions (see strain rate calculation) were constructed from SRTM 90 m DEM data using GeoMapApp. Each of the topographic data profiles are orientated NE–SW and are separated along-strike by 5 km intervals. Spot heights along the topographic profiles are sampled approximately every 850 m. The 5 km width transects were combined to calculate the mean elevation within wider transects (10km, 20km, 30km etc.) to derive regional elevation variations along strike. The 95% confidence intervals of the mean elevation are calculated using the assumption of a normal distribution in the topographic spot heights[10]. Remnants of a flat palaeolandscape, formed close to sea-level during the Pliocene and now identified at high elevations, plus preservation of uplifted marine deposits and terraces indicate that the present day topography has mainly formed since extension began[10]. Subsequent erosion/deposition is minimal and many of the high elevation hanging-wall

basins remain unincised[12]. See Supplementary material for more details. Stress (MPa) and effective viscosity ($\eta = \sigma/2\dot{e}$) (top axis in Fig. 1d) are derived using $\sigma = \rho g h$ where $\rho = 2800$ kgm^{-3} and h = elevation in meters.

Correlation between strain rate and elevation: Grey lines in Fig. 1d are best fit regressions through data obtained by sampling mean elevation, h, and strain rate, $\dot{e}$, in 30 km wide transects (90km across strike). Data from two transect positions (offset by 15 km) are presented to demonstrate there is no selection bias. Regressions lines (Fig. 1d) are given by: $\dot{e} = 10^{-17.8} h^{3.2}$ with $R^2 = 0.8$ (1σ) and $\dot{e} = 10^{-17.9} h^{3.3}$ with $R^2 = 0.9$ (1σ). The estimate of the power law exponent depends on transect width; 30 km wide transects best constrain its value (see Fig. S2). The six different transect positions at this scale yield a value of the exponent in the range 3.0 to 3.3 and a pre-factor of $10^{-17.6+0.3-0.9}$. We use $\dot{e} = 10^{-17.6} h^{3.2}$ in Figure 4 to predict the variation in strain rate from topography.

Temperature-depth calculation: We use values for Q, log A, R and n (Eqn. 1) from a flow law for wet quartz[26] and solve for the temperature T that predicts strain rates of similar magnitude to those measured across 5 km wide fault zones[9]. $Q = 135 \pm 15$ kJ/mol, log $A = -11.2 \pm 0.6$ MPa^{-n}/s, $R = 8.314472$ m^2 kg s^{-2} K^{-1} mol^{-1}, $n = 4$**.** We obtain $T = 710 \pm 120$ K, i.e., ~440 ±120°C. Average surface heat flow of 50 mWm^{-2} in this area[15] is used to derive temperature versus depth through the upper crust assuming a surface temperature of 10°C, crustal heat production = 1 x 10^{-6} Wm^{-3} and thermal conductivity = 2.5 J s^{-1} m^{-1} K^{-1}. Following the standard approach, crustal heat production decreases exponentially with depth (characteristic depth = 10 km). The inferred depth range of viscous flow implied by the temperature range is 25±7.5 km, i.e., below the depth extent of upper crustal seismicity (14-

214 17 km[19, 21]). As mantle lithosphere is thinned in this region, extrapolating this temperature
215 depth profile may underestimate lower crust/upper mantle temperatures.

216

217 **Reference**s

218 1. Thatcher, W. Nonlinear strain build up and the earthquake cycle on the San Andreas
219 Fault, *J. Geophys. Res*., **88**, 5893–5902 (1983).
220 2. Bürgmann, R. & Dresen, G. Rheology of the lower crust and upper mantle: Evidence
221 from rock mechanics, geodesy and field observations. *Ann. Rev. Earth Planet. Sci*., **36**,
222 531–567 (2008).
223 3. Kenner, S. J. & Simons, M. Temporal clustering of major earthquakes along individual
224 faults due to post-seismic reloading, *Geophys. J. Int*, **160**, 179-194 (2005).
225 4. Freed, A. M. Earthquake triggering by static, dynamic and postseismic stress transfer,
226 *Ann. Rev. Earth Planet Sci.* **33**, 335-367 (2005).
227 5. Carter, N. L. & Tsenn, M. C. Flow properties of continental lithosphere. *Tectonophysics*,
228 **136**, 27–63 (1987).
229 6. Newman R. & White N. The dynamics of extensional sedimentary basins: constraints
230 from subsidence inversion, *Philos. Trans. R. Soc. Lond*. **357**, 805– 830, (1999).
231 7. Freed, A. M. & Bürgmann, R. Evidence of power law flow in the Mojave Desert mantle.
232 *Nature*, **430**, 548–551 (2004).
233 8. Handy, M. R., Hirth, G. & Bürgmann, R. Continental fault structure and rheology from
234 the frictional viscous transition downward. In: *Tectonic Faults: Agents of Change on a*
235 *Dynamic Earth*. (Edited by: Handy, M. R., Hirth, G. and Hovius, N.). MIT Press
236 Cambridge Massachusetts, London, UK, pp. 139–181 (2007).

9. Faure Walker, J.P., Roberts, G.P., Sammonds, P.R., & Cowie, P. A. Comparison of earthquake strains over 10^2 to 10^4 year timescales: Insights into variability in the seismic cycle in central Apennines, Italy., *J. Geophys. Res.,* **115**, B10418, (2010).
10. Faure Walker, J. P., Roberts, G. P., Cowie, P. A., Papanikolaou, I., Michetti, A. M., Sammonds, P., Wilkinson, M., McCaffrey, K.J. & R.J. Phillips, Relationship between topography and strain rate in the actively extending Italian Apennines. *Earth Planet. Sci. Lett*., **325/326**, 76–84, (2012).
11. Roberts, G. P. & Michetti, A. M. Spatial and temporal variations in growth rates along active normal fault systems: an example from The Lazio–Abruzzo Apennines, central Italy. *J. Struct. Geol.*, **26,** 339-376 (2004).
12. D'Agostino, N., Jackson, J., Dramis, F., Funiciello, R. Interactions between mantle upwelling, drainage evolution and active normal faulting: an example from the central Apennines (Italy). *Geophys. J. Int*. **147**, 475–497 (2001).
13. D'Anastasio, E., De Martini, P.M., Selvaggi, G., Pantosti, D., Marchioni, A. & Maseroli, R. Short-term vertical velocity field in the Apennines (Italy) revealed by geodetic levelling data. *Tectonophysics,* **418**, 219–234 (2006).
14. D'Agostino, N., Mantenuto, S., D'Anastasio, E., Giuliani, R., Mattone, M., Calcaterra, M., Gambino, P., and Bonci, L. Evidence for localized active extension in the central Apennines (Italy) from global positioning system observations. *Geology*, **39**, 291–294, (2011).
15. Della Vedova, B., Bellani, S., Pellis G. & Squarci, P. Deep temperatures and surface heat flow distribution, in *Anatomy of an Orogen: The Apennines and adjacent Mediterranean Basins* (*eds*. G. B. Vai & I. P. Martini). Kluwer Academic Publishers. pp. 65-76 (2001).
16. England, P. & Molnar, P. Late Quaternary to decadal velocity fields in Asia. *J. Geophys. Res.*, **110**, B12401 (2005).

17. Flesch, L. & Bendick, R. The relationship between surface kinematics and deformation of the whole lithosphere. *Geology*, 40, 711-714 (2012).

18. Naliboff, J. B., Lithgow-Bertolloni, C., Ruff, L. J. & de Koker, N. The effects of lithospheric thickness and density structure on Earth's stress field. *Geophys. J. Int.*, **188**, 1–17 (2008).

19. Boncio, P., Tinari, D. P., Lavecchia, G., Visini, F. & Milana, G. The instrumental seismicity of the Abruzzo Region in Central Italy (1981-2003): seismotectonic implications, *Ital.J.Geosci.* (Boll.Soc.Geol.It.), **128**, 367-380, (2009).

20. Jaeger, J. C. & Cook, N.G. Fundamentals of rock mechanics, 2nd Edition, Chapman & Hall, London, 593 pp. (1979).

21. Chiarabba, C. and 28 co-authors. The 2009 L'Aquila (central Italy) M_w6.3 earthquake: Main shock and aftershocks. *Geophys. Res. Let*., **36**, L18308 (2009).

22. Huismans, R.S. & Beaumont, C. Roles of lithospheric strain softening and heterogeneity in determining the geometry of rifts and continental margins, *In* Karner, G.D., Manatschal, G., & Pinhiero, L.M. (eds) Imaging, Mapping and Modelling Continental Lithosphere Extension and Breakup, pp. 107-134. *Geol. Soc. Lond. Spec. Pub.*, **282**, (2007).

23. Fusseis, F., Handy, M. R. & Schrank. Networking of shear zones at the brittle-to-viscous transition (Cap de Creus, NE Spain), *J. Struct. Geol*., **28**, 1228-1243 (2006).

24. Ellis, S. & Stöckhert, B. Imposed strain localization in the lower crust on seismic timescales, *Earth Planets Space*, **56**, 1103-1109, (2004).

25. Mehl, L. & Hirth, G. Plagioclase recrystallization and preferred orientation in layered mylonites: Evaluation of flow laws for the lower crust, *J. Geophys. Res*., **113**, B05202, (2008).

26. Hirth, G., Teyssier, C. & Dunlap, W.J. An evaluation of quartzite flow laws based on comparisons between experimentally and naturally deformed rocks, *Int. J. Earth Sci.,* (Geologishe Rundschau), **90**, 77-87 (2001).

27. Platt, J. P. & Behr, W. M. Grainsize evolution in ductile shear zones: Implications for strain localisation and the strength of the lithosphere. *J. Struct. Geol*., **33**, 537-550 (2011).

28. Gliozzi, E. & Mazzini, I. Paleoenvironmental analysis of Early Pleistocene brackish marshes in the Rieti and Tiberino intraappenninic basins (Latium and Umbria, Italy) using ostracods (Crustacea). *Palaeogeogr. Palaeoclimatol. Palaeoecol*. 140, 325–333 (1998).

29. Mancini, M. D'Anastasio, E., Barbieri, M. & De Martini, P-M. Geomorphological, paleontological and $^{87}Sr/^{86}Sr$ isotope analyses of early Pleistocene paleoshorelines to define the uplift of Central Apennines (Italy). *Quaternary Research,* **67,** 487–501 (2007).

30. Roberts, G. P., Michetti, A., Cowie, P. A., Morewood, N. C. & Papanikolaou, I. Fault Slip-Rate Variations During Crustal-Scale Strain Localisation, Central Italy. *Geophys. Res. Lett.*, **29**, 1168, (2002).

Supplementary Information:

Section 1: Summary of main calculation steps used in strain rate calculations plus evaluation of sources and magnitudes of uncertainties.

Section 2: Estimate of power law exponent relating strain rate to elevation using different transect widths and positions including an analysis of confidence intervals on these estimates.

Section 3: Comparing depth extent of active seismicity to inferred depth of viscous flow for different values of surface heat flow measured in the Italian Apennines.

Correspondence and requests for materials should be addressed to P.A. Cowie (patience.cowie@geo.uib.no)

Acknowledgements. N. D'Agostino supplied the long wavelength topography data used in Figs. 2 and 4. This work was supported by NERC grants: NER/S/A/2006/14042, NE/E01545X/1 and NE/I024127/1. Financial support was also provided by the Statoil Earth System Modelling project (P.S.) and the Statoil-University of Bergen Akademia agreement (P.C.). We thank R. Huismans for useful discussions and P. Molnar, M. Handy and an anonymous reviewer for their comments.

Author contribution statement:

PAC led the interpretation of the scaling exponent in terms of mid-crustal shear zones.

CHS contributed to understanding the behaviour of coupled frictional-viscous fault systems.

GPR provided the structural data and analysed the strain rate vs elevation relation.

JFW performed the strain rate calculations and quantified data uncertainties.

PS contributed to understanding stress and strain rate variations in a layered lithosphere.

Figure 1. **Correlation between Holocene-averaged regional extensional strain rates and mean elevation along the Italian Apennines**. (**a**) Location map, (**b**) fault pattern overlying SRTM DEM, (**c**) strain rate (red) and elevation (black) versus distance measured every 10 km in 90 km transects across strike. Shading indicates 1σ error. (**d**) Log-log plot of h, stress (MPa), effective viscosity ($\eta = \sigma/2\dot{e}$), versus $\dot{e}$ for two independent data sets (triangles, diamonds), offset by 15km along strike, using 30km wide transects. Grey lines: best fit power laws (1σ error). Grey dashed lines: 99% CI for all transect widths and positions (see Supplementary material).

Figure 2. Spatial variation in strain rate with elevation across the central Apennines (Abruzzo). (**a**) Pattern of normal faults (red lines) superimposed on long wavelength topography (m) (black contours). Grey shading >800 m. Thick red lines: faults where Holocene slip rate exceeds long term rate[30]. Holocene extensional strain rates (blue bars) in grid cells 20 km x 20 km[9]. Grid orientated parallel to principal strain axes. (**b**) Topographic slope vs. change in strain rate (black dots) between adjacent 20 km grid cells along the maximum extension orientation from NE to SW; open circles indicate where a cell contains no faults.

Figure 3. Rheology and loading of a coupled frictional-viscous fault system. (**a**) Schematic fault geometry and rheological structure. FVT = Frictional-Viscous Transition. Strain rate enhancement (red line) depends on shear zone width (5 km assumed here). (**b**) Brittle-frictional-viscous components loaded in parallel by a driving stress that depends on elevation, h. Both components may deform elastically on short time scales. Frictional element A represents (collectively) the seismogenic faults, viscous element B the corresponding viscous (mylonitic) shear zones. (**c**) Distribution of crustal stress (and strength) at yield and the increase in differential stress, due to regional uplift, which leads to deformation.

Figure 4. Contemporary strain accumulation across Abruzzo. Width of high strain rate zone (along line shown in Fig. 2a) implied by geodesy[14] (red arrow) (current resolution: $\dot{e} \geq 2 \times 10^{-8}$) versus fault scarp mapping (blue arrow) (estimated resolution: $\dot{e} \geq 5 \times 10^{-9}$). Strain rate variation (grey line) predicted from long wavelength topography[14] (thick black line) using $\dot{e} = 10^{-17.6} h^{3.2}$ (see Methods). Thin black line: SRTM topography. Stars indicate locations of large historical earthquakes (1915 Fucino Ms = 7.0 and 2009 L'Aquila Mw = 6.3). Dashed line: width of active zone inferred from earthquake shaking records since 1349.

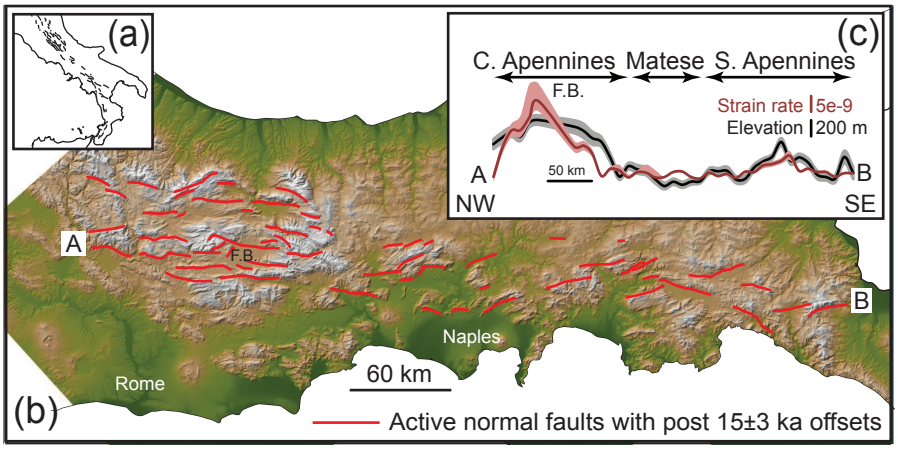
(a)
(b)
(c)
C. Apennines
Matese
S. Apennines
F.B.
Strain rate 5e-9
Elevation 200 m
50 km
A
B
NW
SE
Naples
Rome
60 km
Active normal faults with post 15±3 ka offsets

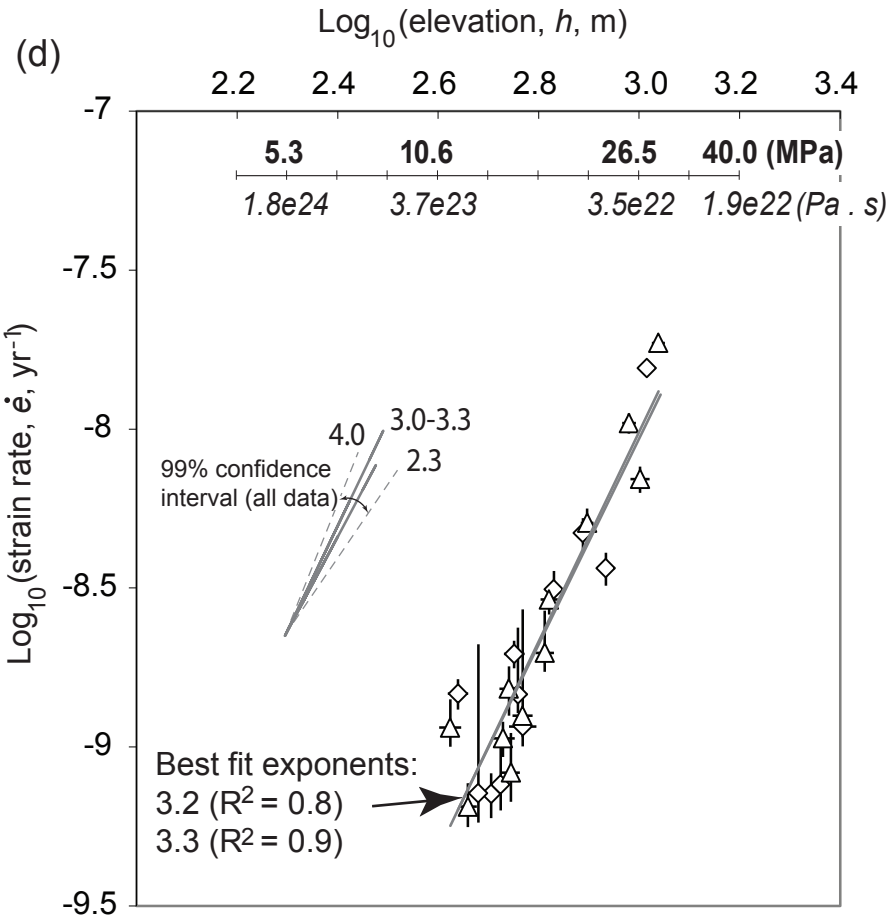
(d)
Log10(elevation, h, m)
2.2
2.4
2.6
2.8
3.0
3.2
3.4
-7
-7.5
-8
-8.5
-9
-9.5
5.3
10.6
26.5
40.0 (MPa)
1.8e24
3.7e23
3.5e22
1.9e22 (Pa . s)
Log10(strain rate, ė, yr-1)
4.0
3.0-3.3
2.3
99% confidence
interval (all data)
Best fit exponents:
3.2 (R2 = 0.8)
3.3 (R2 = 0.9)

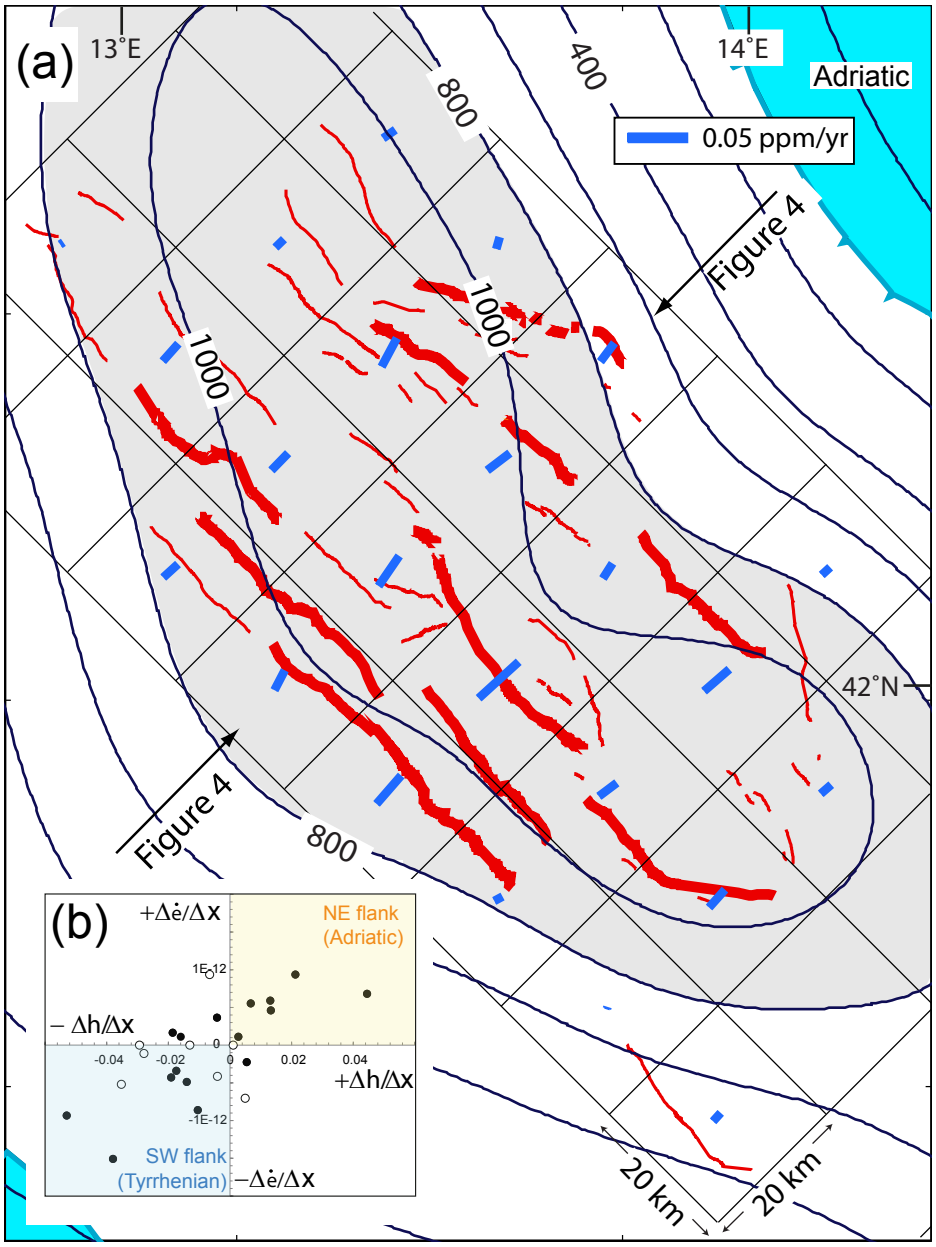
(a)
13°E
14°E
Adriatic
400
800
1000
1000
0.05 ppm/yr
Figure 4
42°N
Figure 4
800
(b)
+Δė/Δx
NE flank
(Adriatic)
1E-12
– Δh/Δx
-0.04
-0.02
0
0.02
0.04
+Δh/Δx
-1E-12
SW flank
(Tyrrhenian)
–Δė/Δx
20 km
20 km

Figure 2

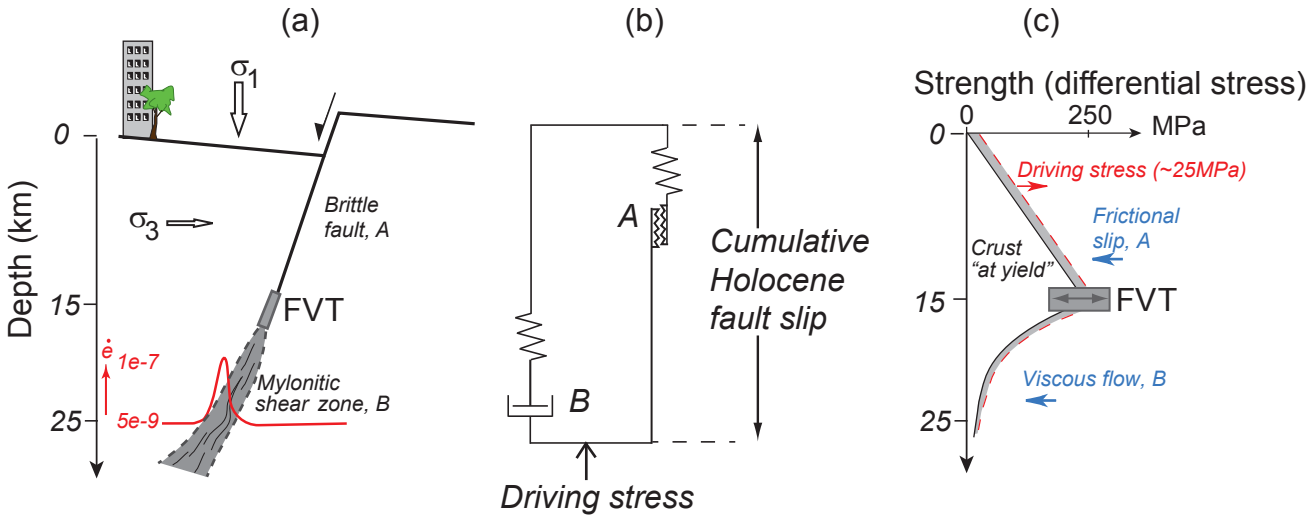
(a)
(b)
(c)
σ1
σ3
0
15
25
Depth (km)
Brittle
fault, A
FVT
ė 1e-7
5e-9
Mylonitic
shear zone, B
A
B
Cumulative
Holocene
fault slip
Driving stress
Strength (differential stress)
0
250
MPa
Driving stress (~25MPa)
Frictional
slip, A
Crust
"at yield"
FVT
Viscous flow, B

Figure 3

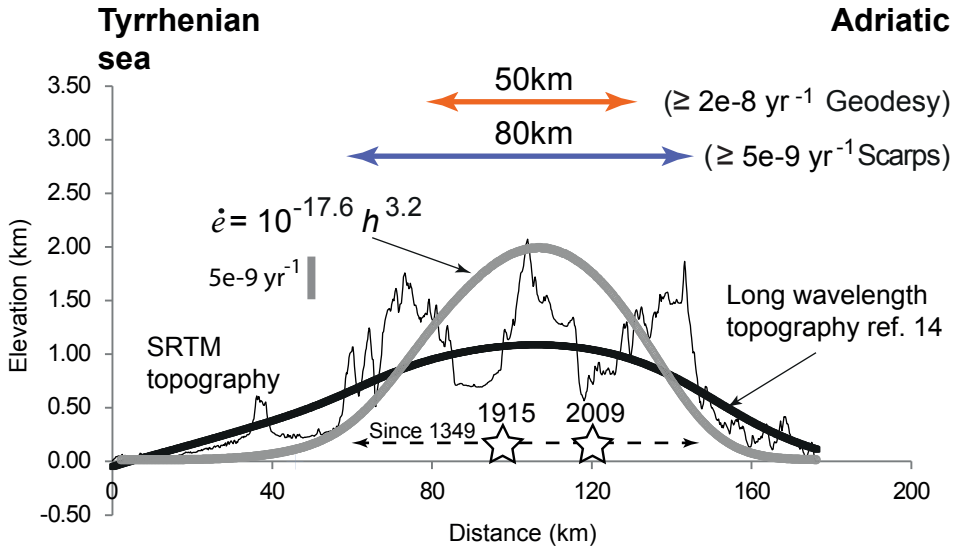
Tyrrhenian sea
Adriatic
50km
(≥ 2e-8 yr -1 Geodesy)
80km
(≥ 5e-9 yr -1 Scarps)
ė = 10-17.6 h 3.2
5e-9 yr-1
SRTM topography
Long wavelength topography ref. 14
Since 1349
1915
2009
Elevation (km)
Distance (km)
3.50
3.00
2.50
2.00
1.50
1.00
0.50
0.00
-0.50
0
40
80
120
160
200

Figure 4